Progress in Additive Manufacturing
https://doi.org/10.1007/s40964-021-00167-5

FULL RESEARCH ARTICLE

Additive manufacturing of Ti-6Al-4V alloy by metal fused filament fabrication (MF^3): producing parts comparable to that of metal injection molding

Paramjot Singh[1] · Vamsi K. Balla[1,2] · Azim Gokce[1,3] · Sundar V. Atre[1] · Kunal H. Kate[1]

Received: 19 July 2020 / Accepted: 19 January 2021

Abstract
This paper presents metal-fused filament fabrication (MF^3) for manufacturing Ti-6Al-4V parts by 3D printing of green parts followed by debinding and sintering to obtain mechanical properties comparable to metal injection-molded (MIM) specimens. The current work discusses critical material and process aspects of the MF^3 process that currently limits it from effective defect-free translation from 3D printed to sintering. We show successfully produced bound filament with 59 vol% of Ti-6Al-4V powder mixed with a polymeric binder system to print parts using MF^3. The feedstock and filaments showed uniform powder dispersion and acceptable flowability necessary for consistent extrusion during MF^3 printing, leading to defect-free parts. The green part density was $98.5 \pm 0.6\%$ relative to the density of the 59 vol% Ti-6Al-4V feedstock that resulted in successful debinding without slumping, no warpage, and layer delamination of the MF^3 parts. A two-step debinding combining solvent and thermal extraction of polymer binder followed by sintering in partial vacuum resulted in almost isotropic shrinkage of ~ 14% in all directions. The sintered density of these parts was $94.2 \pm 0.1\%$. The mechanical properties of the present MF^3 processed Ti-6Al-4V alloy parts represent UTS of 875 ± 15 MPa and elongation of $17 \pm 3\%$, which being 1.7% higher in UTS and 17.5% higher in elongation when compared to literature data for metal injection-molded parts.

Keywords Metal-fused filament fabrication (FFF) · Ti-6Al-4V 3D printing · Sintering · Mechanical properties · Microstructure

1 Introduction

Metal-fused filament fabrication (MF^3) is a hybrid additive manufacturing technique which essentially combines green part fabrication by fused-filament fabrication (FFF) and thermal processing of metal injection molding (MIM). As per ASTM terminology, the MF^3 process falls under material extrusion additive manufacturing (MEAM). MF^3 can offer several advantages compared to existing metal AM processes, such as laser powder bed fusion (L-PBF), direct energy deposition (DED), and electron beam melting (EBM). Some examples of potential benefits include: (i) significantly lower capital cost, (ii) the absence of high rapid heating/cooling rates and directional heat extraction enables elimination of residual stresses, provide equiaxed grains and more isotropic microstructures and mechanical properties (iii) elimination of handling loose powder during printing (iv) improved powder recyclability during net-shaping due to lower process temperatures at the green state, (v) well-known debinding and sintering knowledge from metal injection molding, (vi) possibility to print non-weldable metals and brittle ceramics, (vii) multi-material printing capability in one part, (viii) potential to fabricate parts in space, where the use of other powder-bed-based AM processes poses serious powder and bed stability concerns [1, 2].

This study's overall MF^3 process is presented in Fig. 1. It shows various parts, such as a bracket, spinal implant, NASA insignia, and automotive brake lever, produced from the current work at both green and sintered stage. Here, the feedstock filaments are made using powder-binder mixtures

✉ Kunal H. Kate
kunal.kate@louisville.edu

[1] Materials Innovation Guild, University of Louisville, Louisville, KY 40208, USA

[2] Bioceramics and Coating Division, CSIR-Central Glass and Ceramic Research Institute, Kolkata 700032, India

[3] Sakarya University of Applied Sciences, 54187 Sakarya, Turkey

Published online: 11 February 2021

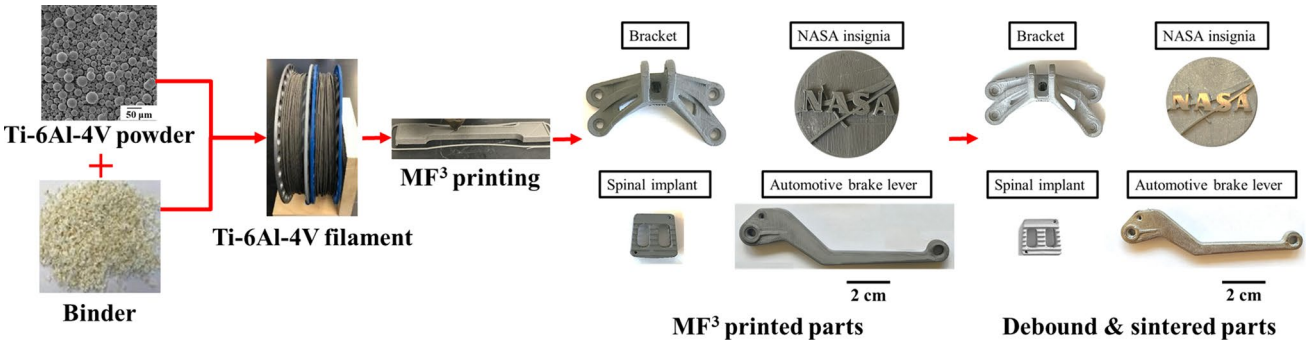

Fig. 1 Overview of the MF^3 process used in the present study to fabricate Ti-6Al-4V parts

and printed using a desktop FFF printer. Thermal processing by debinding followed by sintering is used to produce robust and net shape metal components. The work on MEAM-based processes report back to 1996, where researchers from Rutgers University led the efforts for metal (17-4 PH stainless steel) and ceramic 3D printing (Si_3N_4) [3, 4]. However, the filaments were found to be straight, stiff, and not flexible enough to be spooled. A significant amount of porosity, printing defects, and delamination and cracking were also reported after debinding and sintering. Later some printing parameter optimization has been reported to eliminate some of these defects in the green parts [5]. Although some understanding of the feedstock material properties for printing has been developed [6], the effect of processing and printing parameters on green part properties, sintered properties, and microstructure was absent in these earlier studies [7]. However, in the last 5 years, the interest in MEAM-based processes, particularly MF^3, has surged, and several variations of the MF^3 process using polymer-metal feedstocks have been reported [1, 2, 8, 9]. Commercial machines are currently available from Markforged (ADAM™: atomic diffusion additive manufacturing) and Desktop Metal (BMD™: bound metal deposition) with a claimed capability to process 17-4PH, 316L, H13, A2, D2 tool steels, Cu, Inconel 625 alloy parts [10, 11]. However, the scientific understanding of the materials and parameters at each step of the MF^3 process (Fig. 1) is still incomplete and not available in the open literature.

In the open literature, we found that the MF^3 has been used to print various metals, including 17-4PH stainless steel, 316L stainless steel, W–Cr, WC–Co [2, 8, 9, 12]. Gonzalez-Gutierrez et al. [9] reported tensile properties of 17-4PH stainless steel printed with polymer-metal powder bound filaments, achieving sintered ultimate tensile strength (UTS) of 695 ± 35 MPa with $3.8 \pm 1.9\%$ elongation at break. When compared to MIM literature, these properties were lower by 35% in UTS and 50% in elongation; the reason for such discrepancy was attributed to print defects leaving pores and insufficient layer adhesion. Damon et al. [13] performed fused filament fabrication of 316L stainless steel producing parts with 93% of UTS and 61% elongation compared to the MIM process. Through microstructural observations, the print process-induced pores were held responsible for the reduction in obtained properties. Lengauer et al. [12] investigated polymer-WC–Co filaments for printing intricate geometries and reported only on the sintered shrinkage of $21 \pm 1\%$. The microstructure revealed pores presence resulting from the printing process, with no mention of the resulting physical and mechanical properties. However, most of these studies only provide a general overview of the feasibility of the MF^3 process to create metal parts.

Ti-6Al-4V alloy has a combination of properties (such as high specific strength to weight ratio, biocompatibility, good corrosion resistance) that makes it an excellent material of choice for automotive, medical, and aerospace applications. As a result, significant amounts of research have been done on AM of this alloy using processes including L-PBF, EBM, and DED [14]. The localized heating and extreme thermal gradients in these processes lead to high residual stresses, which in turn, govern the macrostructure and the microstructures of printed parts [14]. The inevitable defect formation and directional property anisotropy are still a constraint with these AM routes [15, 16]. Table 1 lists some of the common physical and mechanical properties of Ti-6Al-4V alloy produced with metal injection molding (MIM), laser powder bed fusion (L-PBF), and wrought (Ti-6Al-4V).

Interestingly, the use of MF^3 to process Ti and its alloys is very scarce in the literature except for a brief study by Zhang et al. [17]. They have used filaments with 55 vol% powder loading, and the printing parameters appear to be not optimized, which resulted in a significant amount of porosity and printing defects in the sintered parts (relative density of ~ 91%). Further, the debinding of such porous parts is relatively less challenging than fully density parts due to their high surface area to volume ratio. Finally, the mechanical properties of sintered parts were not reported except hardness determined using nanoindentation.

Table 1 Properties of Ti-6Al-4V components fabricated using several manufacturing routes

Process	Relative density (%)	Yield strength (MPa)	Ultimate tensile strength (MPa)	Elongation (%)	Source
MIM	97.3 ± 1.2	750 ± 25	860 ± 40	14 ± 4	[18–22]
L-PBF	99.7 ± 0.15	1150 ± 80	1270 ± 70	6 ± 2	[23–25]
Wrought (annealed)	100	830 ± 10	930 ± 10	13 ± 1.5	[26]

We believe that for successful printing and design of metal-polymer mixtures for use in MF^3, five key considerations, such as (1) high powder loading, (2) homogeneous powder-binder distribution, (3) sufficient filament stiffness, (4) low viscosity during printing, and (5) no binder residue before sintering, must be taken into account. Typically, a high powder loading (> 50 vol%) is expected to reduce slumping during debinding and shrinkage during sintering. On the other hand, a very high powder loading could result in inconsistent printing due to hindrance in feedstock flow through the printing nozzle. Similarly, non-uniform powder dispersion in the polymer matrix can pose processing difficulties due to large fluctuations in the viscosity and associated pressure changes in the nozzle leading to inconsistent printing. In the MF^3 process, the filament is driven into the heated liquefier by a knurled roller, where it acts as a plunger to force the material through the nozzle. Therefore, sufficient filament strength and stiffness are necessary to avoid filament breakage while entering the nozzle [27]. It was also found that the size of the powder in metal-polymer filament strongly affects their flexibility, strength, and hence the printability and printing speed [28]. Further, improper selection of print extrusion parameters can lead to poor layer/bead adhesion and generate voids between printed beads, resulting in low green density and poor structural integrity of printed parts [29–31]. Moreover, the printing process is directly affected by material viscosity, which changes with temperature and shear rate and composition and the powder-binder ratio [5, 27, 28, 32, 33]. It is also desirable to have high-density green parts, as the presence of large voids and related defects cannot be eliminated during sintering and eventually result in inferior mechanical properties [34]. During debinding, the presence of binder residue can prevent densification, affect microstructures, and produce parts with low properties. The sintering process and environmental control are also equally crucial for obtaining effective microstructure, densification, no distortion, and required properties with MF^3. However, achieving accurate control of the debinding and sintering processes is particularly challenging in MF^3 parts that have high geometric complexity.

To our knowledge, few prior reports have comprehensively examined the feedstock and filament characteristics, print parameters, and debinding and sintering outcomes, which are critical for successful MF^3 processing, particularly for Ti6Al4V alloy. Therefore, in this work, we report successful Ti-6Al-4V parts fabricated using the MF^3 process following effective powder-binder feedstock preparation for filament fabrication. The printing of high-density green parts followed by binder removal and sintering to achieve properties and microstructures comparable to equivalent counter processes, such as MIM, correlated with MF^3 processed Ti-6Al-4V alloy properties.

2 Experimental methods

2.1 Materials

The present work uses a Ti-6Al-4V alloy powder with a median particle size of 30 µm (Praxair Surface Technologies, Indianapolis, Indiana). The as-received powder was characterized for true, apparent, and tap densities to assess flowability and packing density. The true density (ρ) of powder was measured using a helium gas pycnometer (Accupyc II 1340, Micromeritics Inc., GA, USA). The powder's density is determined to ensure the powder is fully dense without a significant amount of porosity inside the powder, which can influence the amount of solids loading in the powder-binder mixtures. The tap density (ρ_t) of powder was measured using a tap density volumeter (AS-100 Tap Density Tester, Aimsizer Scientific, Dandong Liaoning, China) as per ASTM B527-15. The apparent volume of powder (without any mechanical tapping) was measured in a cylinder and divided by its mass to obtain the apparent density (ρ_a). The powder's constituent phases were identified by analyzing the X-ray diffraction (XRD) pattern (Discovery D8 HR, BRUKER AXS, Inc., USA).

The binder composition used to prepare the filament feedstock consisted of three components, including a backbone polymer (30–50 wt%), an elastomer (20–30 wt%), and a plasticizing phase (20–40 wt%). The backbone component serves a twofold purpose: first, by providing the necessary strength and stiffness to the filament, and second, in assisting component shape retention during thermal debinding. The elastomer provides flexibility to the filament such that it can be spooled into coils for the ease of printing and storage. The plasticizing phase helps decrease feedstock viscosity and improve overall metal powder loading into the binder matrix.

2.2 Feedstock preparation and characterization

The solids loading in a feedstock is the ratio of the volume of metal powder to the powder and binder's total volume in a feedstock. The critical solids loading was determined using a torque rheometer (IntelliTorque Plasti-Corder, C. W. Brabender Instruments, Inc. NJ, USA). An initial batch (500 g) with 58 vol% powder-binder mixture was blended and introduced at 180 °C, followed by mixing with a blade rotating speed of 100 rpm. The mixing torque was monitored until it stabilized, indicating homogeneous mixing. Subsequently, the additional powder was added in increments of 1 vol% (up to 67 vol%) each time until the torque stabilized. The mixing torque was monitored with each addition until a sharp rise in torque, which indicates the critical solids loading.

Based on the critical solids loading, determined as above, a solids loading of 59 vol% was selected for preparing the feedstock filaments for further MF^3 printing using the mixing conditions reported above. The mixing torque was monitored to evaluate the mixture homogeneity of the feedstock until it became stable at 45 min of mixing. Viscosity measurements as a function of shear rate and temperature were also performed for this feedstock using a capillary rheometer (Rheograph 20, GÖTTFERT Werkstoff-Prüfmaschinen GmbH, Germany) with a tungsten carbide die (*L*/*D* ratio of 30:1). The feedstock viscosity was measured at 240 °C for shear rates between 20 and 800 s^{-1}, to understand the shear rate and temperature effects on feedstock viscosity. Feedstock homogeneity was determined by measuring time-dependent variations in viscosity at a constant shear rate and temperature [35]. In the current study, a constant shear rate of 50 s^{-1} at 160 °C was used to evaluate the variations in feedstock viscosity to measure its homogeneity. Additionally, powder concentration post mixing was also evaluated by measuring the feedstock's pycnometer density in granule and filament forms. For this purpose, the feedstock sampling was carried out by taking random portions of the same batch to correlate with the initial volume of powder added to the feedstock.

2.3 Filament extrusion and MF^3 printing

The 59 vol% Ti-6Al-4V feedstock was extruded into filaments with a consistent diameter of 1.75 ± 0.05 mm using a capillary die with an *L*/*D* ratio of 30/1.75 mm on a capillary rheometer. The extrusion temperature was 105 °C with a uniform extrusion speed of 0.1 mm/s with pressure measured at the capillary entrance corresponding to 40 ± 3 MPa. The filament properties were evaluated in terms of ultimate tensile strength, Young's modulus, and elongation using tensile tests (Universal Testing Machine EZ-SX, Shimadzu Inc., Kyoto, Japan) to assess material printability. All tests were conducted at 20 °C, with a load cell of 500 N at a strain rate of 0.001 s^{-1}. Enough care was taken to ensure no filament slip occurred in the gripping section during the test. The Young's modulus was determined from the slope of the stress–strain curve.

Table 2 lists the selected parameters for printing parts (Pulse 3D Printer, Matterhackers, Lake Forest, CA, USA) using the MF^3 process based on several printing experiments performed using our feedstock system. Our initial experiments showed that an extrusion temperature of 240 °C enabled consistent material flow due to optimal feedstock viscosity during printing. Similarly, a bed temperature of 65 °C resulted in good adhesion of the part to the build platform during the entire printing process. A layer height of 150 µm with 100% infill selected to achieve close packing of printed beads leading to dense green parts. The selected bead deposition angle of alternating 0° and 90° resulted in sound and dense parts. While a print speed of 10 mm s^{-1} resulted in good infill, consistent material flow (at extrusion multiplier of 115%), and strong inter-bead and inter-layer bonding, this could not be achieved higher printing speeds.

2.4 Debinding and sintering

A two-step debinding procedure was used to reduce thermal debinding time and debinding-related defects while completely removing the binder components. In this method, MF^3 printed green parts were first solvent debound in n-heptane solution at 64 °C for 4 h. Then, the samples were dried overnight in an oven at 80 °C to remove the residual solvent. The thermal debinding profile was developed using thermal degradation data of solvent debound samples generated using a thermogravimetric analyzer (TGA, SDT Q600, TA Instruments, New Castle, DE, USA). Thermogravimetric analysis (TGA) experiments were performed with a heating rate of 2 °C/min up to 550 °C in an N_2 atmosphere. The samples' thermal debinding was carried out in a partial vacuum of 600 mTorr with argon sweep (Super Series Vacuum Furnace, TM Vacuum Products Inc., Cinnaminson, NJ, USA) using a heating rate of 1 °C/min. For complete polymer binder removal, four holds were used at 250 °C, 330 °C,

Table 2 MF^3 printing parameters were used in this investigation to fabricate Ti-6Al-4V parts

Filament extrusion temperature	240 °C
Print bed temperature	65 °C
Layer height	150 µm
Infill	100%
Fill angle	0°, 90°
Print speed	10 mm s^{-1}
Nozzle diameter	400 µm
Extrusion multiplier	115%
Outer perimeter loops	3

440 °C, and 550 °C with a dwell/soaking time of 3 h, 3 h, 4 h, and 4 h, respectively. Thermally debound samples were sintered in the same furnace using a partial vacuum of 150 millitorrs at 1250 °C for 4 h with argon as cover gas and a heating rate of 3 °C/min.

2.5 Physical, mechanical, and microstructural characterization

The printed parts were characterized for green density using the Archimedes principle and analyzed for pore distribution along the cross section using a scanning electron microscope. For relative density calculations, the pycnometer density of feedstock at 59 vol% (3.01 g/cm^3), and Ti-6Al-4V powder (4.43 g/cm^3) were used as a basis. The density of sintered parts was also determined using the Archimedes principle. The mechanical properties of sintered tensile test coupons (ASTM E8) were determined using a tensile testing machine (Hydraulic Tensile Testing Machine, MTS Systems Corporations, Eden Prairie, Minnesota, USA) with 100 kN load cell at a strain rate 0.001 s^{-1} using an extensometer to measure the elongation in the gauge length. For microstructural analysis, sintered samples were polished using SiC papers in the sequence of 120/240/400/600/800/1200 followed by 1 µm diamond slurry and then colloidal silica slurry. The sintered samples' cross section was etched using Kroll's reagent to reveal microstructural features and was observed under an optical microscope (Olympus BX-51, Olympus Corporations, Shinjuku City, Tokyo, Japan). Additional phase analysis was performed using an XRD analyzer, and the fracture surfaces were analyzed to correlate with the resulting properties, using a Scanning Electron Microscope (TESCAN Vega3 SEM, TESCAN Inc., Brno, Czech Republic).

3 Results and discussion

3.1 Metal powder characteristics

Figure 2 shows the XRD peaks of as-received Ti-6Al-4V alloy powder, and peaks primarily correspond to hexagonal close-packed α-Ti. No noticeable amounts of β-Ti peaks were identified, primarily due to rapid cooling rates during the gas atomization process, which restricted the formation of β in the powder and is in agreement with published work [36]. The spherical morphology of the Ti-6Al-4V powder was confirmed by SEM and is shown as an inset in Fig. 2.

The powder was found to have 90% of the particles < 44 µm based on the manufacturer's particle size distribution. Table 3 summarizes experimentally determined packing attributes for Ti-6Al-4V powders. As shown in Fig. 2 (inset), the powders were spherical and such powders

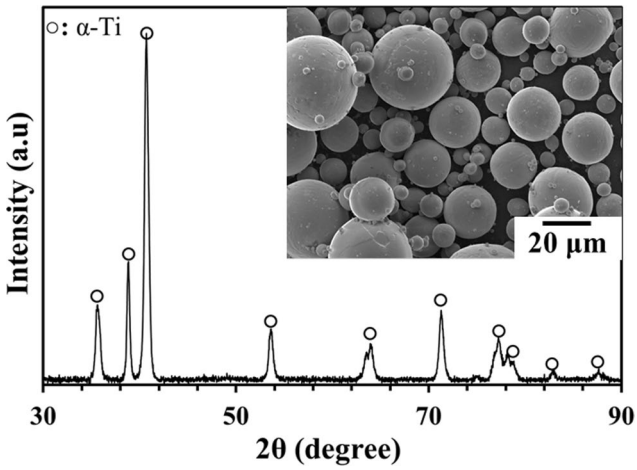

Fig. 2 X-ray diffraction pattern for Ti-6Al-4V powder shows a major phase as α-Ti with an inset of the SEM image revealing spherical powder morphology

Table 3 Characteristics of Ti-6Al-4V alloy powder used in this investigation

D_{10} (µm)	2
D_{50} (µm)	30
D_{90} (µm)	44
Pycnometer density, ρ (g/cm^3)	4.43 ± 0.002
Apparent density, ρ_a (g/cm^3)	2.54 ± 0.005
Tap density, ρ_t (g/cm^3)	2.75 ± 0.03

are known to provide improved flowability and high packing density, which is critical for MF^3 3D Printing. A higher powder packing density allows more powder addition into a feedstock mixture, reducing the overall shrinkage during sintering. The powder packing fraction can be theoretically determined from the ratio of powder ρ_t to ρ [37] and for the powder under investigation, it was found at 0.62.

Additionally, a high value of powder flowability is expected to decrease the feedstock viscosity by providing the least resistance to flow within the polymer binder matrix, making 3D printing easier at high solids loadings. Therefore, to understand the powder flow a Hausner ratio (ρ_t to ρ_a) of present powder was determined. The current powder has a Hausner ratio of 1.08, and the ratio < 1.2 is often considered to provide acceptable powder flowability in powder-based manufacturing.

4 Metal powder-polymer feedstock characteristics

Selecting appropriate powder loading in the polymer matrix is extremely critical as excessive solids loading can result in high viscosity, which adds to print obstructions and failure,

and entrapment of air pockets in the green parts [1, 6]. At the same time, too much binder increases the chances of part slumping during debinding and high shrinkage during the sintering of parts made using such powder-polymer feedstocks [38]. Figure 3a shows the effect of metal powder addition on the mixing torque during feedstock preparation. It can be seen that from 59 to 64 vol%, the torque increased by increments of 0.4 ± 0.2 N m for every 1 vol% increment in the powder addition. This trend is indicative of increased inter-particle friction with increased solid loading in the powder-binder feedstock mixture. However, the mixing torque abruptly increased $> 2.4 \pm 0.2$ N m, with an increase in the solids loading beyond 64 vol%. This transition is indicative of a mixture with a less available binder to homogeneously coat each powder particle, resulting in excessive direct particle contacts and inter-particle friction [37, 38]. For the current powder-binder system, the critical loading was determined to be 64 vol%. The powder solids loading was selected at 59 vol% to ensure good feedstock flowability and viscosity during the MF^3 printing process, based on several preliminary experiments.

The viscosity of 59 vol% Ti-6Al-4V feedstock was determined at 240 °C in the shear rate range of 20–800 s^{-1}. Rabinowitsch correction was applied to the apparent shear rate to determine the shear rate at the wall. As shown in Fig. 3b, the viscosity decreased with an increase in shear rate. The increasing shear rate from 20 to 800 s^{-1} showed a decrease in the viscosity from 475 ± 10 to 55 ± 2 Pa s. In MF^3, the viscosity and subsequent pressure drop in the heated nozzle depend on several factors, such as the powder loading, binder composition, feed rate, temperature, and heat transfer gradients (temperature drops) in the heated liquefier and nozzle sections. Anderegg et al. [27] experimentally verified the temperature drop at the exit of the heated liquefier, leading to increased viscosity and a high-pressure differential. Such a pressure drop can result in non-uniform material extrusion during printing, leaving air gaps between deposited beads and bonded layers. The pressure drop is also dependent on the feedstock material homogeneity and powder loading. With the current Ti-6Al-4V feedstock at 59 vol% loading, a printing temperature of 240 °C was used to achieve feedstock viscosity that facilitates consistent printing. FFF systems typically operate at shear rates < 300 s^{-1} [39] depending on the feedstock materials, filament feed rate, etc. There exists a limit to the feed rate where if the extrusion force exceeds the shear strength of the filament at the roller feeding mechanism, the filament fails at the entrance [28]. A slow printing speed of 10 mm s^{-1} is found to ensure low feed rates that allow consistent printing using current Ti-6Al-4V filaments.

The homogeneity of feedstock plays an essential role during printing and ensures consistent printing with uniform distribution of powder across the printed parts. Agglomeration of powder in the feedstock can lead to filament breakage during handling or printing. On the other hand, filaments with regions lean in powder invariably produce low powder areas that can slump, shrink, and cause warpage, porosity, etc. during thermal processing. Therefore, the feedstock homogeneity was accessed for variations in viscosity at a constant shear rate of 50 s^{-1} and a temperature of 160 °C. The feedstock viscosity measurement was repeated for eight data points, and it was observed that the feedstock viscosity remained at 730 Pa s with a standard deviation of ± 2 Pa s. This small deviation in the feedstock viscosity and the resulting coefficient of variation below 0.5% clearly indicate that the feedstock is highly homogeneous. The viscosity variation assessment was consistent with the inferences from the variations in pycnometer density of the feedstock, 2.96 ± 0.002 g cm^{-3}, which was in close agreement with the estimated density based on the inverse rule-of-mixtures (~ 3 g cm^{-3}) [40].

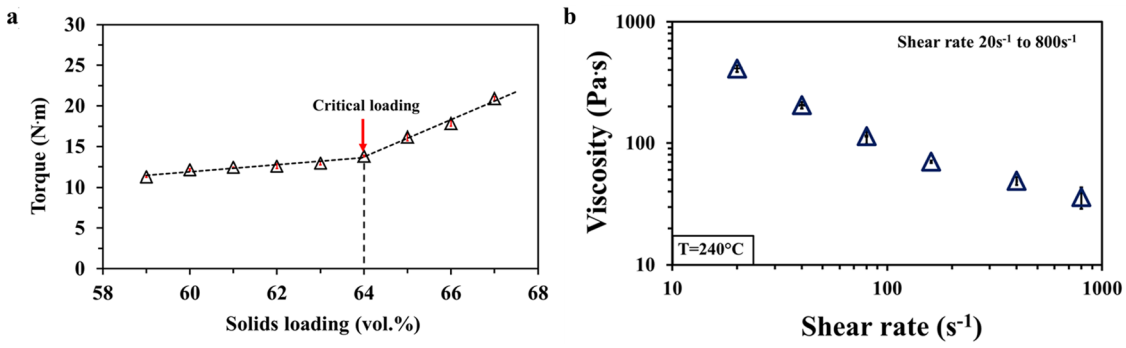

Fig. 3 **a** Effect of solids loading on mixing torque, **b** influence of shear rate on the viscosity of Ti-6Al-4V feedstock (59 vol%) prepared in this work

5 Filament properties

The green filament was produced from 59 vol% Ti-6Al-4V feedstock and characterized for density using the Archimedes principle. A 100% filament relative density was achieved to the feedstock's pycnometer density (2.96 ± 0.002 g cm^{-3}). High filament density is essential to achieve uniform stiffness and reduce the chances of breaking during printing [28]. Further, it enables easy and consistent extrusion of material by maintaining a constant pressure during deposition. Therefore, high filament density always translates into high green part density, consistent material extrusion, and uniform part density.

The filaments were also analyzed for defects and other inconsistencies using SEM along the cross section and outer surface. As shown in Fig. 4a, b, the powder was found to be homogeneously dispersed in the polymer matrix with no noticeable presence of voids. The cross section of the filament was also found to be circular (∅ 1.75 ± 0.05 mm), and none of the filament batches showed ovality. The dark spots in Fig. 4a are the regions of pulled out powder, which appear dark due to their topography. At higher magnification, an excellent powder-polymer interface with numerous adhesion/contact points on the powder can be clearly seen in Fig. 4c. This powder-polymer interface is expected to provide sufficient mechanical strength to the filaments and enable uniform flow. Figure 4d, e shows the outer surface of the filament. The surface was found to be smooth without any gross defects, which can reduce the strength of the filament. The surface also appears to be covered with polymer and some regions of exposed metal powder (Fig. 4e, f), possibly contributing to the excellent filament flexibility that improves resistance to surface damage during handling and feeding through the printer. Further, the smooth surface reduces backpressure from friction with the guide tube through which filament passes before entering the heated liquefier. The Young's modulus, ultimate tensile strength, and elongation of the current filament were 170 ± 20 MPa, 1.15 ± 0.15 MPa, and of 2.2 ± 0.5%, respectively. The filament was also found to be flexible and easily woundable on a spool of a desktop printer.

6 MF^3 printing

The printed parts were analyzed for their dimensions and compared to the actual CAD part dimensions to understand the parts expansion or contraction after printing. Figure 5a shows a tablet and an ASTM tensile specimen with dimensions, and Fig. 5b (Top) shows the sliced file that directs the nozzle travel around the bed to create the entire 3D geometry. Figure 5b (bottom) shows typical green parts printed using a Pulse FFF printer. Table 4 lists the difference in the printed part and the actual CAD part dimensions, which was within 0.5%. The parts geometric tolerances depend on the motion-controlled by the gantry system, selection of process parameters, and printed material properties. In the gantry system, the stepper motor's step size controls the accuracy and details to which a CAD model is translated into a built part. As shown in Table 4, the resulting difference was positive (parts larger than respective designs) along the XY plane. Since the material coming through the nozzle flows laterally and the die swelling phenomenon occurs as the melt leaves the printer nozzle, resulting in radial expansion of extrudate, which affects dimensions and limits the resolution considerations of FFF parts [41].

As the layer thickness (150 µm) is less than the diameter of the nozzle (400 µm), the material is squeezed through the print nozzle over the print bed or previous layer leading to broader deposited beads. The part dimensions in *X*/*Y* directions also depend on other process parameters, such as the extrusion multiplier and printing speed. Similarly, the layer thickness, bead width, and the feed rate are some of the other governing parameters that strongly affect the part's final dimensions. Interestingly, the dimensional change was negative along the printing direction (*Z* direction). One of the possible reasons could be the thermal contraction of the printed layers upon cooling. Printing material composition and its thermo-physical properties like viscosity, specific volume, thermal conductivity, and specific heat are expected to have a strong influence on the final geometry. Understanding material properties and its relation to the process parameters can further enable improvements in dimensional control and defect avoidance during printing [42].

In addition to dimensional analysis, the density of the printed parts was also determined. It was found that all samples had a green density of 98.5 ± 0.6% relative to the density of the feedstock. Figure 5c shows typical SEM images of a fractured surface of a green tensile bar along the YZ plane. It can be seen that none of the surfaces have visible macroscale voids and printing defects. The slightly lower density of ~ 1% in the printed parts is believed to be internal pores generated during the printing process, as the green filament was found to be fully dense (100%). Magnified microstructures of green parts in different regions (at the center and the fillet section in Fig. 5c) revealed uniform dispersion of metal powder within the polymer binder throughout the part.

All powder particles were found to be covered with the polymer binder that is critical in achieving uniform feedstock flow through the nozzle during MF^3 printing. Further, such uniform distribution of metal powder and polymer binder in the printed green part could help achieve enough green

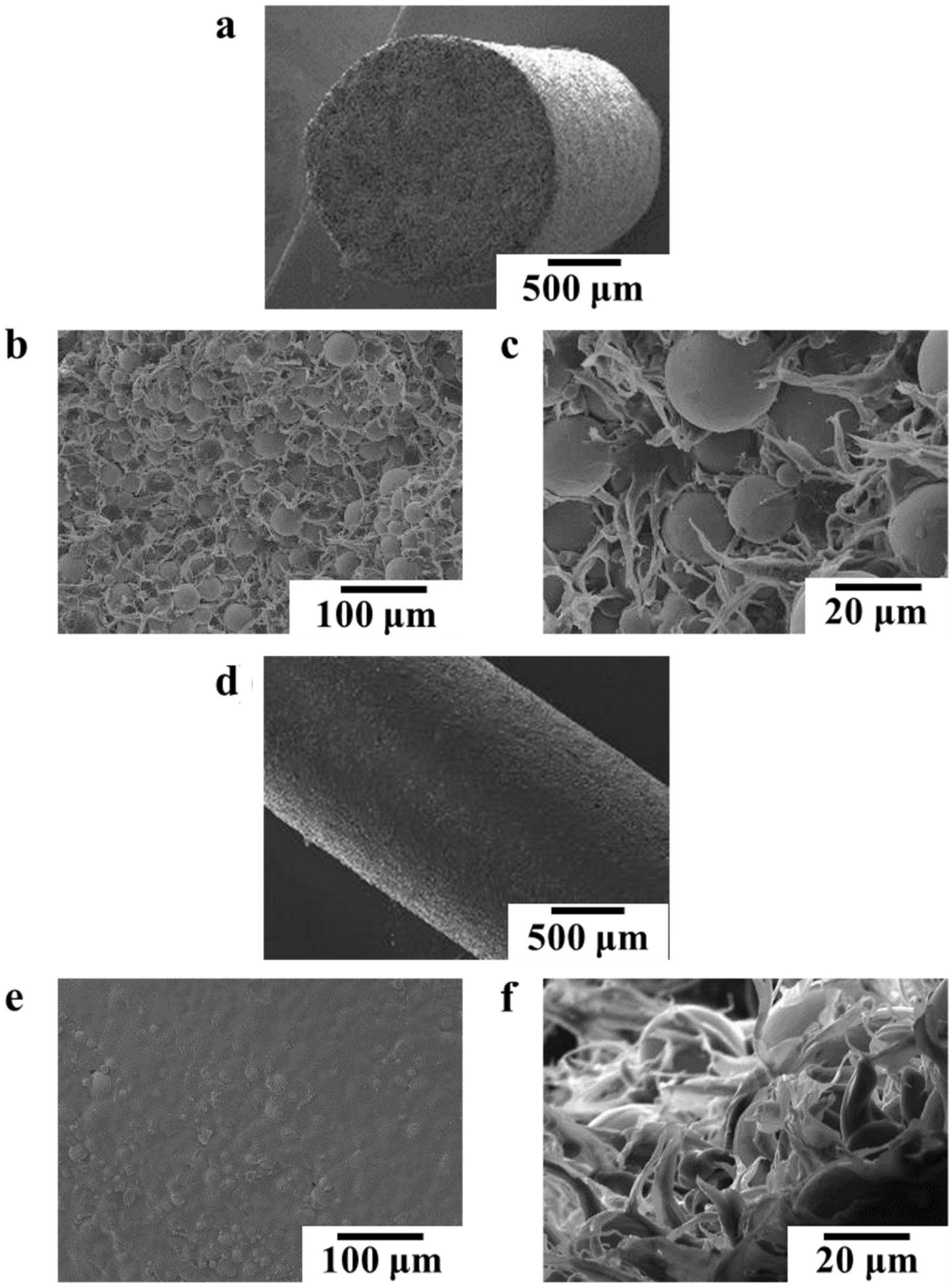

Fig. 4 SEM images of the filament showing powder distribution (**a**, **b**), powder-polymer interface (**c**), and filament surface morphology at different magnifications (**d–f**)

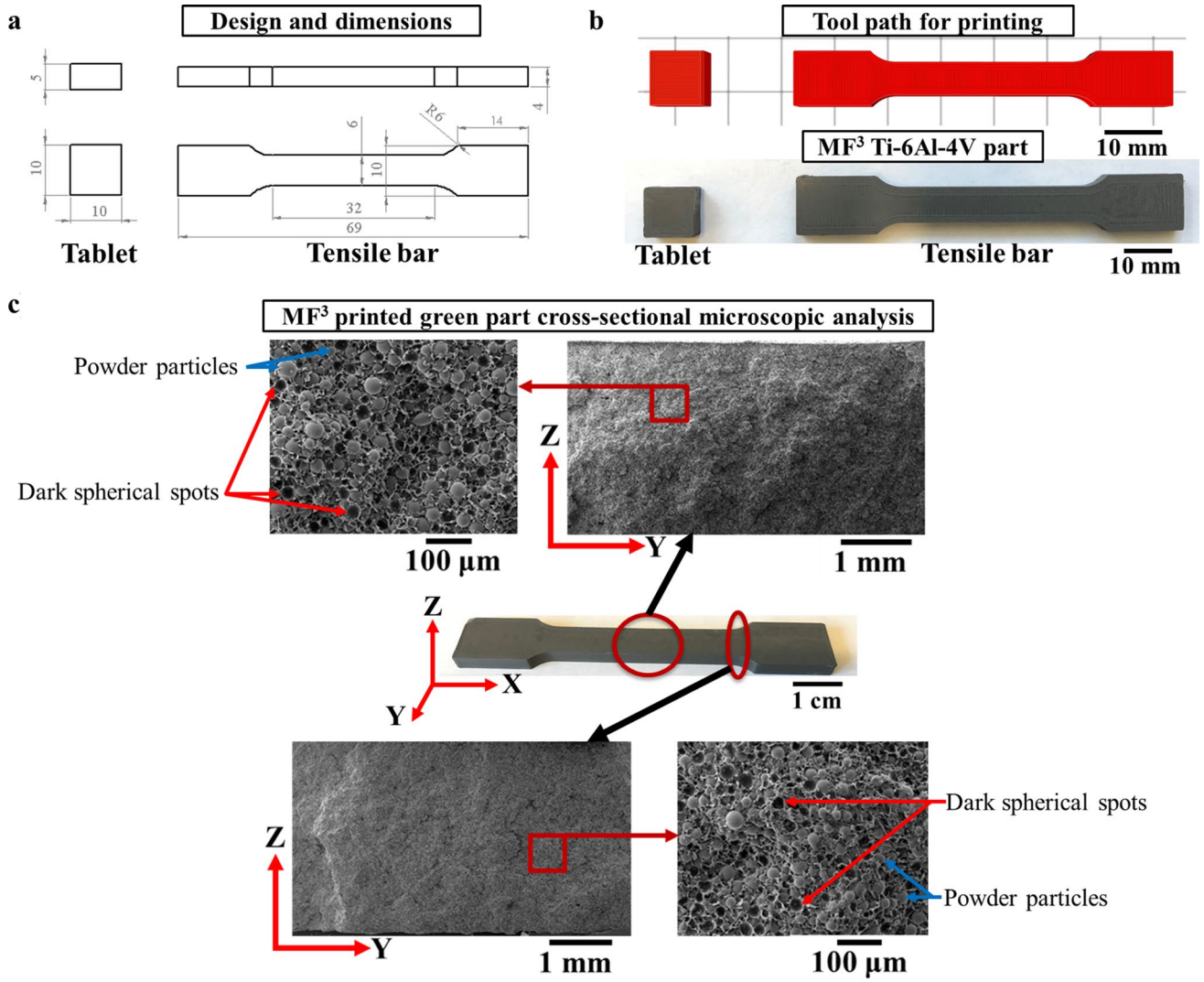

Fig. 5 **a** Design and dimensions of the testing samples, **b** tool path can be recognized in the upper red figure, the bottom figure shows MF^3 printed tablet and tensile bar in a green state, **c** SEM of fractured green part surfaces revealing uniform powder-polymer distribution and absence printing defects, pores (dark spherical spots indicating the regions of particle pullout during specimen fracture for characterizations)

Table 4 Dimensional tolerances of the green Ti-6Al-4V parts ($n=4$) printed using the MF^3 process

Direction	Printed part dimensions		% deviation from the CAD part[a]	
	Tablet	Tensile bar	Tablet	Tensile bar
X	10.05 ± 0.05	69.2 ± 0.15	0.5	0.3
Y	10.03 ± 0.02	6.03 ± 0.02	0.3	0.5
Z	4.97 ± 0.02	3.98 ± 0.01	− 0.5	− 0.7

[a]CAD part dimensions available in Fig. 5, and % deviation expressed for the average of the dimensions

strength (for handling) and more uniform binder removal and shrinkage during debinding and sintering steps, respectively. It is vital to note that these surfaces were devoid of any inter-bead and interlayer delamination even after manually fracturing the green samples. This behavior demonstrates that the bonding between the layers and between the adjacent beads is robust. Previous studies with unfilled polymer parts, printed using FFF, have suggested that residual voids could be eliminated by adjusting several factors, such as layer height, nozzle diameter, volumetric print speed, and material extrusion temperature [43–45]. For example, for the same extrusion and printing speed, low layer height is expected to push more material laterally and reduce voids. In the present investigation, the nozzle diameter is selected based on the desired feature resolution, the particle size of filler, and the

desired pressure drop to maintain uniform flow. Increasing volumetric print speed increases the amount of extrudate being driven out through the nozzle and, therefore, can reduce existing voids. Increasing the printing temperature reduces viscosity and allows a better flow of material.

7 Debinding and sintering

Following preliminary analysis of several experiments using different time–temperature combinations, the optimal conditions for solvent debinding were 64 °C for 4 h in the n-heptane solution, which removed ~ 40% of the total binder. The remaining binder was thermally removed using a temperature profile determined using TGA data. Figure 6a presents the TGA of present feedstock, which revealed polymer binder breakdown in three stages (represented by zones 1–3 in Fig. 6a). The peaks from the weight loss rate denote the temperature at which maximum binder removal is reached. The debinding temperatures were selected from the midpoint of each decomposition zone of TGA data, which were 250 °C, 330 °C, and 440 °C. Figure 6b shows the combined debinding–sintering cycle employed for Ti-6Al-4V feedstock and a hold time of 3 h was used for the initial two zones, with each eliminating 20 wt% of the remainder binder post solvent debinding, the remaining 60 wt% of the binder was removed at 440 °C having hold time of 4 h. A final hold was implemented at 550 °C for 4 h, to ensure all the organic compounds are entirely eliminated. Complete removal of the binder is the most critical part of the entire process. Any residual impurities (typically carbon) can easily react with titanium to form carbides at elevated temperatures, thereby reducing ductility [46]. The debinding cycle was followed by sintering in the same furnace at a temperature of 1250 °C for 4 h with partial vacuum and continuous argon flow to minimize oxidation. Table 5 shows part sintered properties, with current conditions achieved a relative density of 94.2 ± 0.1% with an average shrinkage of 14.5 ± 0.5% in all three directions (X–Y-Z). The shrinkage appears to be isotropic in all three directions, which can be attributed to uniform powder distribution in the green part as a result of homogeneous feedstock/filament use in addition to optimal printing parameters.

8 Mechanical properties and microstructure

Four sintered Ti-6Al-4V parts produced by MF^3 were found to exhibit an ultimate tensile strength (UTS), yield strength, and elongation of 875 ± 15 MPa, 745 ± 10 MPa, and 17 ± 3%, respectively. The stress–strain curves for the test samples are shown in Fig. 7a. We could not compare our mechanical property of MF^3 processed Ti-6Al-4V alloy with other extrusion-based AM technologies as no reported literature data is available. These properties were comparable to the properties of MIM Ti-6Al-4V parts, as shown in Table 1. Figure 7b shows a property comparison of MF^3 against other processing routes used to manufacturing Ti-6Al-4V parts. The properties collected from MIM studies are comparable to MF^3 with UTS and elongation lower on average by 1.7% and 17.5%, respectively. Due to MIM's close similarity

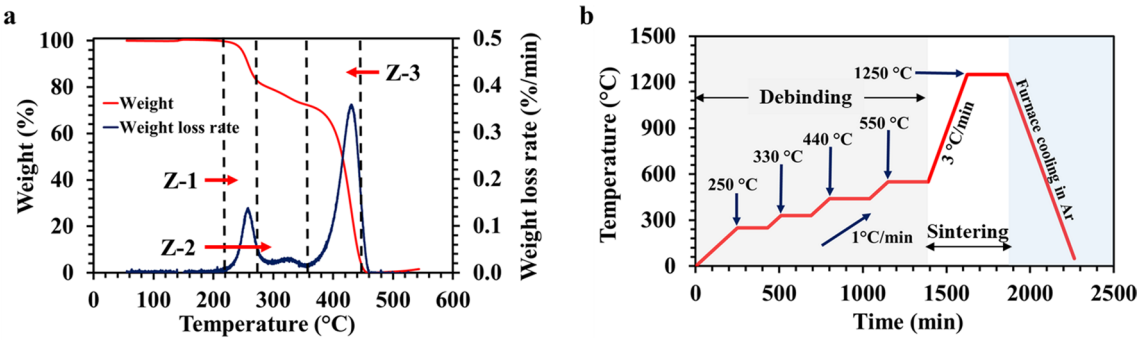

Fig. 6 **a** Thermogravimetric analysis of the Ti-6Al-4V to understand polymer decomposition, **b** debinding and sintering profile for Ti-6Al-4V MF^3 parts

Table 5 Physical and mechanical properties of sintered MF^3 Ti-6Al-4V parts ($n = 4$)

Density (%)	Shrinkage (%)			Yield strength (MPa)	Ultimate tensile strength (MPa)	Elongation (%)
	X	*Y*	*Z*			
94.2 ± 0.1	14 ± 0.5	15 ± 0.5	15 ± 0.5	745 ± 10	875 ± 15	17 ± 3

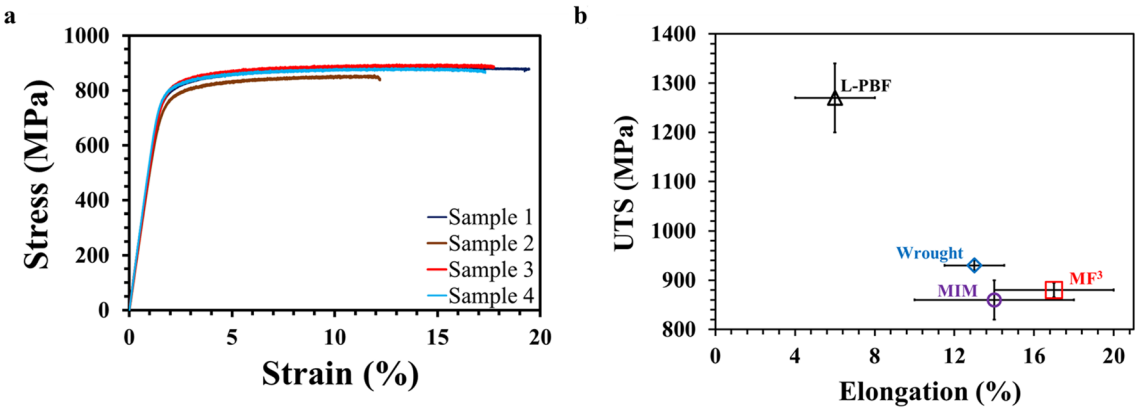

Fig. 7 **a** Stress–strain curve for the MF^3 sintered samples, **b** MF^3 properties compared to conventional routes for processing Ti-6Al-4V alloy

with MF^3 process steps, such as debinding and sintering, the properties appear to be comparable.

However, the important consideration is that in MIM pressures are several orders of magnitude higher than those involved in MF^3 printing of these parts. These results clearly demonstrate that the use of homogeneous feedstock with appropriate solids loading and optimal MF^3 printing parameters can produce Ti-6Al-4V parts with mechanical properties comparable to that of MIM parts. The L-PBF data for UTS was 45% higher than MF^3 but 65% lower in elongation. The microstructural changes occurring leading to such properties in L-PBF are a well-discussed phenomenon that is attributed to the high heat gradients present, which essentially prevents the formation of the β phase [25, 26, 47], with microstructure dominated by the α'-martensitic plates. We have measured the interstitial concentration in the sintered sample, and it was found that under present experimental conditions, the oxygen content was 0.2 ± 0.01 wt% (ASTM standard < 0.2 wt%) and the carbon content was 0.14 ± 0.01 wt% (ASTM standard < 0.08 wt%) in the MF^3 processed Ti-6Al-4V alloy parts. Compared to staring powder oxygen and carbon concentration of 0.08 wt% and 0.01 wt%, these values were found to increase during the MF^3 processing. The oxygen pickup for Ti alloys at elevated temperatures is unavoidable due to titanium's high reactivity [48]. Still, careful control in maintaining a low impurity level is achieved using a combination of inert gas flow as the surrounding environment, zirconia base trays, and low sintering temperatures that produce Ti-6Al-4V parts with permissible concentrations set by ASTM.

Similarly, the carbon concentration was found to increase by 0.13% compared to the starting powder. These carbon concentrations post sintering are related to the polymer binder constituents used in this work. As reported in MIM, the carbon concentration post sintering has always been found to exceed the starting powder carbon concentration, due to the presence of the binder decomposed products post debinding and which can take part in the sintering step [49]. In the future, the focus would be to develop binders that can decompose completely, leaving behind minimal to no residue.

Figure 8a shows the XRD pattern for the phases present in the sintered Ti-6Al-4V alloy. Bragg's peaks pertaining to hexagonal close-packed α-Ti, and body-centered cubic β-Ti peaks were identified. The feedstock powder contained only α-Ti (Fig. 2), but during sintering sufficient amount of β-Ti was formed due to slow heating and cooling rates (Fig. 6b). The microstructures of the sintered tensile bar along different planes were collected and shown in Fig. 8b. In all cross-sectioned planes, the microstructures consisted of typical α + β phases of Ti-6Al-4V alloy with the presence of intergranular β lamella (prior β) marked in Fig. 8b. The prior β grain size was determined using the linear intercept method (ASTM E112-13) and found to be 230 ± 20 µm. The higher magnification image reveals the Widmanstatten microstructure, primarily consisting of α and β lamellae [18]. No printing-induced defects were found in the microstructures, but a measurable number of spherical, isolated pores were observed. The observed pores correlate well with the sintered density of ~ 94%. The tensile fracture surfaces were analyzed using SEM, shown in Fig. 8c, to understand the fracture behavior and the influence of residual porosity on the fracture. The fracture surfaces were found to exhibit clear, fine dimples throughout the sample surface, which are characteristic features of ductile mode of fracture. The presence of residual pores can also be seen from these fractographs, although the fracture origin could not be identified from these images.

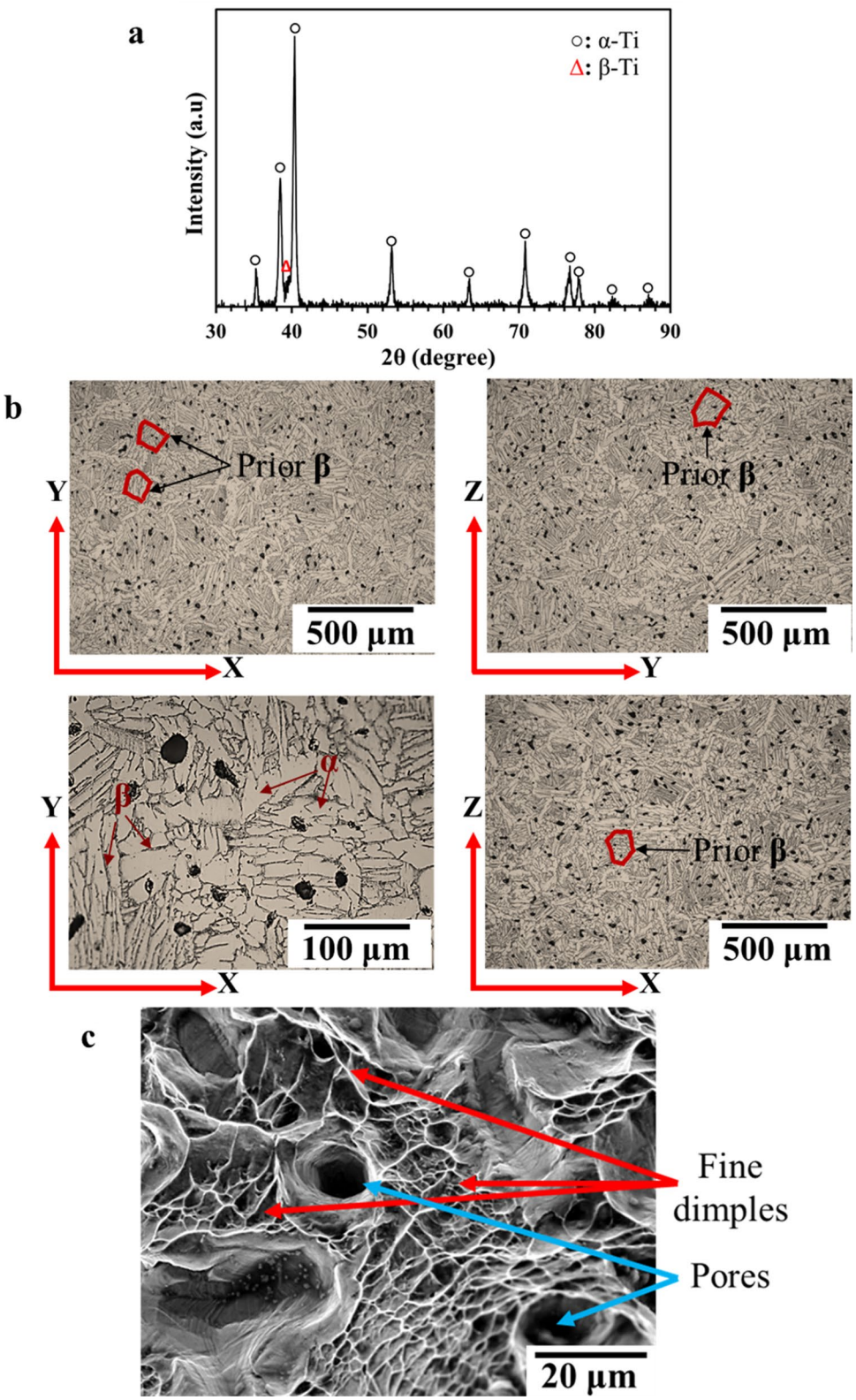

Fig. 8 **a** XRD analysis of the sintered samples exhibiting α and β phases, **b** sintered and polished part microstructure along *XY–YZ–XZ* plane, highlighting Widmanstatten microstructure (for *X–Y–Z* orientation refer Fig. 5), **c** fracture surface of the tensile tested sample showing the presence of fine dimples, consistent with a ductile fracture

9 Conclusions

This study successfully demonstrated the preparation of homogeneous polymer-Ti-6Al-4V alloy feedstock and filaments that were 3D printed using the MF^3 process followed by thermal processing to produce strong Ti-6Al-4V alloy parts. Polymer-bound continuous filament with 59 vol% of Ti-6Al-4V powder was found to exhibit a

density of 2.96 ± 0.002 g cm^{-3}, and Modulus and UTS of 170 ± 20 MPa, 1.15 ± 0.15 MPa, respectively. These stable properties resulted in continuous material extrusion to produce dense green parts with a density of 2.92 ± 0.002 g cm^{-3} (98.5 ± 0.6% relative to that of feedstock density of 2.96 g cm^{-3}). The uniform powder-polymer distribution for filament and then the printed parts yields to facilitate uniform part shrinkage during the sintering. The parts were sintered to a density of 4.2 ± 0.004 g cm^{-3} (94.1 ± 0.1% relative) with an ultimate tensile strength of 875 ± 15 MPa, yield strength of 745 ± 10 MPa, and 17 ± 3% elongation, which are comparable to metal injection-molded Ti-6Al-4V parts. Microstructure analysis indicated the presence of α and β phases with isotropic grain size across the part volume with an average grain size of 230 ± 20 µm. Fractographic analysis of tensile test samples clearly showed a ductile mode of fracture. Our results clearly demonstrate the capability of the MF^3 process to fabricate complex Ti-6Al-4V parts with mechanical properties comparable to that of MIM parts when homogeneous feedstock with appropriate solids loading and optimal MF^3 printing parameters are used.

Acknowledgements The authors acknowledge the support provided through a subcontract from NASA as part of the NASA FABLAB project. Support from the Minority Business Development Agency of the US Department of Commerce and the University of Louisville is also acknowledged.

Compliance with ethical standards

Conflict of interest The authors declare no conflicts of interest.

References

1. Gonzalez-Gutierrez J, Cano S, Schuschnigg S, Kukla C, Sapkota J, Holzer C (2018) Additive manufacturing of metallic and ceramic components by the material extrusion of highly-filled polymers: a review and future perspectives. Materials 11(5):840. https://doi.org/10.3390/ma11050840
2. Thompson Y, Gonzalez-Gutierrez J, Kukla C, Felfer P (2019) Fused filament fabrication, debinding and sintering as a low cost additive manufacturing method of 316L stainless steel. Addit Manuf 30:100861. https://doi.org/10.1016/j.addma.2019.100861
3. Agarwala M, Weeren RV, Bandyopadhyay A, Safari A, Danforth S, Priedeman W (1996) Filament feed materials for fused deposition processing of ceramics and metals. In: 1996 International solid freeform fabrication symposium
4. Agarwala M, Weeren RV, Bandyopadhyay A, Whalen P, Safari A, Danforth S (1996) Fused deposition of ceramics and metals: an overview. In: 1996 international solid freeform fabrication symposium
5. Agarwala MK, Jamalabad VR, Langrana NA, Safari A, Whalen PJ, Danforth SC (1996) Structural quality of parts processed by fused deposition. Rapid Prototyp J 2(4):4–19. https://doi.org/10.1108/13552549610732034
6. Rangarajan S, Qi G, Venkataraman N, Safari A, Danforth SC (2000) Powder processing, rheology, and mechanical properties of feedstock for fused deposition of Si3N4 ceramics. J Am Ceram Soc 83(7):1663–1669. https://doi.org/10.1111/j.1151-2916.2000.tb01446.x
7. Wu G, Langrana NA, Sadanji R, Danforth S (2002) Solid freeform fabrication of metal components using fused deposition of metals. Mater Des 23(1):97–105. https://doi.org/10.1016/S0261-3069(01)00079-6
8. Bose A, Schuh CA, Tobia JC, Tuncer N, Mykulowycz NM, Preston A, Barbati AC, Kernan B, Gibson MA, Krause D (2018) Traditional and additive manufacturing of a new tungsten heavy alloy alternative. Int J Refract Met Hard Mater 73:22–28. https://doi.org/10.1016/j.ijrmhm.2018.01.019
9. Gonzalez-Gutierrez J, Arbeiter F, Schlauf T, Kukla C, Holzer C (2019) Tensile properties of sintered 17–4PH stainless steel fabricated by material extrusion additive manufacturing. Mater Lett 248:165–168. https://doi.org/10.1016/j.matlet.2019.04.024
10. Markforged. Metal 3D Printing. https://markforged.com/. Accessed 11 July 2020.
11. Desktop Metal. Metal 3D Printing. https://www.desktopmetal.com/. Accessed 11 July 2020.
12. Lengauer W, Duretek I, Fürst M, Schwarz V, Gonzalez-Gutierrez J, Schuschnigg S, Kukla C, Kitzmantel M, Neubauer E, Lieberwirth C (2019) Fabrication and properties of extrusion-based 3D-printed hardmetal and cermet components. Int J Refract Met Hard Mater 82:141–149. https://doi.org/10.1016/j.ijrmhm.2019.04.011
13. Damon J, Dietrich S, Gorantla S, Popp U, Okolo B, Schulze V (2019) Process porosity and mechanical performance of fused filament fabricated 316L stainless steel. Rapid Prototyp J 25(7):1319–1327. https://doi.org/10.1108/RPJ-01-2019-0002
14. Liu S, Shin YC (2019) Additive manufacturing of Ti6Al4V alloy: a review. Mater Des 164:107552. https://doi.org/10.1016/j.matdes.2018.107552
15. DebRoy T, Wei H, Zuback J, Mukherjee T, Elmer J, Milewski J, Beese AM, Wilson-Heid A, De A, Zhang W (2018) Additive manufacturing of metallic components–process, structure and properties. Prog Mater Sci 92:112–224. https://doi.org/10.1016/j.pmatsci.2017.10.001
16. Kok Y, Tan XP, Wang P, Nai M, Loh NH, Liu E, Tor SB (2018) Anisotropy and heterogeneity of microstructure and mechanical properties in metal additive manufacturing: a critical review. Mater Des 139:565–586. https://doi.org/10.1016/j.matdes.2017.11.021
17. Zhang Y, Bai S, Riede M, Garratt E, Roch A (2020) A comprehensive study on fused filament fabrication of Ti-6Al-4V structures. Addit Manuf. https://doi.org/10.1016/j.addma.2020.101256
18. Ergül E, Özkan Gülsoy H, Günay V (2009) Effect of sintering parameters on mechanical properties of injection moulded Ti–6Al–4V alloys. Powder Metall 52(1):5–71. https://doi.org/10.1179/174329008X271691
19. Nor NM, Muhamad N, Ihsan AM, Jamaludin K (2013) Sintering parameter optimization of Ti-6Al-4V metal injection molding for highest strength using palm stearin binder. Proc Eng 68:359–364. https://doi.org/10.1016/j.proeng.2013.12.192
20. Obasi G, Ferri O, Ebel T, Bormann R (2010) Influence of processing parameters on mechanical properties of Ti–6Al–4V alloy fabricated by MIM. Mater Sci Eng A 527(16–17):3929–3935. https://doi.org/10.1016/j.msea.2010.02.070
21. Shibo G, Xuanhui Q, Xinbo H, Ting Z, Bohua D (2006) Powder injection molding of Ti–6Al–4V alloy. J Mater Process Technol 173(3):310–314. https://doi.org/10.1016/j.jmatprotec.2005.12.001
22. Sidambe A, Figueroa I, Hamilton H, Todd I (2010) Metal injection moulding of Ti-64 components using a water soluble binder. PIM Int 4(4):56–62
23. Qiu C, Adkins NJ, Attallah MM (2010) Microstructure and tensile properties of selectively laser-melted and of HIPed

laser-melted Ti–6Al–4V. Mater Sci Eng A 578:230–239. https://doi.org/10.1016/j.msea.2013.04.099
24. Rafi H, Karthik N, Gong H, Starr TL, Stucker BE (2013) Microstructures and mechanical properties of Ti6Al4V parts fabricated by selective laser melting and electron beam melting. J Mater Eng Perform 22(12):3872–3883. https://doi.org/10.1007/s11665-013-0658-0
25. Vrancken B, Thijs L, Kruth J-P, Van Humbeeck J (2012) Heat treatment of Ti6Al4V produced by Selective Laser Melting: Microstructure and mechanical properties. J Alloy Compd 541:177–185. https://doi.org/10.1016/j.jallcom.2012.07.022
26. Wysocki B, Maj P, Sitek R, Buhagiar J, Kurzydłowski KJ, Święszkowski W (2017) Laser and electron beam additive manufacturing methods of fabricating titanium bone implants. Appl Sci 7(7):657. https://doi.org/10.3390/app7070657
27. Anderegg DA, Bryant HA, Ruffin DC, Skrip SM Jr, Fallon JJ, Gilmer EL, Bortner MJ (2019) In-situ monitoring of polymer flow temperature and pressure in extrusion based additive manufacturing. Addit Manuf 26:76–83. https://doi.org/10.1016/j.addma.2019.01.002
28. Singh P, Balla VK, Tofangchi A, Atre SV, Kate KH (2020) Printability studies of Ti-6Al-4V by metal fused filament fabrication (MF3). Int J Refract Met Hard Mater. https://doi.org/10.1016/j.ijrmhm.2020.105249
29. Wang J, Xie H, Weng Z, Senthil T, Wu L (2016) A novel approach to improve mechanical properties of parts fabricated by fused deposition modeling. Mater Des 105:152–159. https://doi.org/10.1016/j.matdes.2016.05.078
30. Guan HW, Savalani MM, Gibson I, Diegel O (2015) Influence of fill gap on flexural strength of parts fabricated by curved layer fused deposition modeling. Proc Technol 20:243–248. https://doi.org/10.1016/j.protcy.2015.07.039
31. Ziemian S, Okwara M, Ziemian CW (2015) Tensile and fatigue behavior of layered acrylonitrile butadiene styrene. Rapid Prototyp J 21(3):270–278. https://doi.org/10.1108/RPJ-09-2013-0086
32. Ramanath H, Chua C, Leong K, Shah K (2008) Melt flow behaviour of poly-ε-caprolactone in fused deposition modelling. J Mater Sci Mater Med 19(7):2541–2550. https://doi.org/10.1007/s10856-007-3203-6
33. Gurrala PK, Regalla SP (2014) Part strength evolution with bonding between filaments in fused deposition modelling: this paper studies how coalescence of filaments contributes to the strength of final FDM part. Virtual Phys Prototyp. https://doi.org/10.1080/17452759.2014.913400.9(3):141-149
34. German R (2014) Sintering: from empirical observations to scientific principles. Butterworth-Heinemann, Oxford
35. Zauner R, Binet C, Heaney D, Piemme J (2004) Variability of feedstock viscosity and its correlation with dimensional variability of green powder injection moulded components. Powder Metall 47(2):150–155. https://doi.org/10.1179/003258904225015473
36. Jamaludin MI, Kasim NAA, Nor NHM, Ismail MH (2015) Development of porous Ti-6Al-4V Mix with palm stearin binder by metal injection molding technique. Am J Appl Sci 12(10):742. https://doi.org/10.3844/ajassp.2015.742.751
37. Contreras J, Jimenez-Morales A, Torralba J (2010) Experimental and theoretical methods for optimal solids loading calculation in MIM feedstocks fabricated from powders with different particle characteristics. Powder Metall 53(1):34–40. https://doi.org/10.1179/003258909X12450768327225
38. German RM, Bose A (1997) Injection molding of metals and ceramics. Metal Powder Industries Federation, Princeton
39. Gilmer EL, Miller D, Chatham CA, Zawaski C, Fallon JJ, Pekkanen A, Long TE, Williams CB, Bortner MJ (2018) Model analysis of feedstock behavior in fused filament fabrication: enabling rapid materials screening. Polymer 152:51–61. https://doi.org/10.1016/j.polymer.2017.11.068
40. Supati R, Loh N, Khor K, Tor S (2000) Mixing and characterization of feedstock for powder injection molding. Mater Lett 46(2–3):109–114. https://doi.org/10.1016/S0167-577X(00)00151-8
41. Turner BN, Gold SA (2015) A review of melt extrusion additive manufacturing processes: II. Materials, dimensional accuracy, and surface roughness. Rapid Prototyp J 21(3):250–261. https://doi.org/10.1108/RPJ-02-2013-0017
42. Singh P, Shaikh Q, Balla VK, Atre SV, Kate KH (2020) Estimating powder-polymer material properties used in design for metal fused filament fabrication (DfMF3). JOM 72(1):485–495. https://doi.org/10.1007/s11837-019-03920-y
43. Abbott A, Tandon G, Bradford R, Koerner H, Baur J (2018) Process-structure-property effects on ABS bond strength in fused filament fabrication. Addit Manuf 19:29–38. https://doi.org/10.1016/j.addma.2017.11.002
44. Kuznetsov V, Solonin A, Urzhumtsev O, Schilling R, Tavitov A (2018) Strength of PLA components fabricated with fused deposition technology using a desktop 3D printer as a function of geometrical parameters of the process. Polymers 10(3):313. https://doi.org/10.3390/polym10030313
45. Sun Q, Rizvi G, Bellehumeur C, Gu P (2008) Effect of processing conditions on the bonding quality of FDM polymer filaments. Rapid Prototyp J 14(2):72–80. https://doi.org/10.1108/13552540810862028
46. Ebel T, Ferri OM, Limberg W, Schimansky F-P (2011) Metal injection moulding of advanced titanium alloys. Adv Powder Metall Part Mater 1:45–57
47. Murr L, Quinones S, Gaytan S, Lopez M, Rodela A, Martinez E, Hernandez D, Martinez E, Medina F, Wicker R (2009) Microstructure and mechanical behavior of Ti–6Al–4V produced by rapid-layer manufacturing, for biomedical applications. J Mech Behav Biomed Mater 2(1):20–32. https://doi.org/10.1016/j.jmbbm.2008.05.004
48. German R (2009) Titanium powder injection moulding: a review of the current status of materials, processing, properties and applications. PIM Int 3(4):21–37
49. Dehghan-Manshadi A, Bermingham M, Dargusch M, StJohn D, Qian M (2017) Metal injection moulding of titanium and titanium alloys: challenges and recent development. Powder Technol 319:289–301. https://doi.org/10.1016/j.powtec.2017.06.053